CrossMark

Meshfree generalized finite difference methods in soil mechanics—part II: numerical results

I. Michel[1] · S. M. I. Bathaeian[2] · J. Kuhnert[1] ·
D. Kolymbas[2] · C.-H. Chen[2] · I. Polymerou[2] ·
C. Vrettos[3] · A. Becker[3]

Abstract In geotechnical engineering, simulations are of utmost importance. Due to large deformations, meshfree methods are more suitable than classical meshbased methods. Nevertheless, they have to be validated on the laboratory scale in order to guarantee reliable conclusions for real life applications. In this contribution, we complete the theoretical description of the two novel meshfree generalized finite difference methods Finite Pointset Method (FPM) and Soft PARticle Code (SPARC) by numerical results for the standard benchmark problems oedometric and triaxial test. We focus on the quality of the results as well as on the rate-independent character of the numerical implementation of the nonlinear barodesy model for sand.

1 Introduction

As a granular material, soil is often exposed to large, non-topological deformations. Classical meshbased methods struggle in these cases, even if remeshing capacities

---

✉ I. Michel
 isabel.michel@itwm.fraunhofer.de

1 Fraunhofer Institute for Industrial Mathematics ITWM, Fraunhofer-Platz 1, 67663 Kaiserslautern, Germany

2 Division of Geotechnical and Tunnel Engineering, University of Innsbruck, Technikerstr. 13, 6020 Innsbruck, Austria

3 Division of Soil Mechanics and Foundation Engineering, University of Kaiserslautern, P.O. Box 3049, 67653 Kaiserslautern, Germany

⧍ Springer

are used. Due to their intrinsic characteristic, discretization without fixed connectivities, meshfree methods enjoy great popularity. In Chen et al. (2017), the progress of meshfree techniques during the last 20 years is described with special focus on large deformation problems. These techniques can be separated into five categories: generalized finite element methods (GFEM), generalized finite volume methods (GFVM), generalized finite difference methods (GFDM), discrete element methods (DEM), and generalized mass point methods (GMPM). Making no claim to be complete, applications in geomechanics can be found e.g. in Abe et al. (2017), Bandara and Soga (2015), Bardenhagen et al. (2000), Beuth et al. (2011, 2013), Bhandari et al. (2016), Blanc (2008), Blanc and Pastor (2013), Bui and Fukagawa (2011), Bui et al. (2015), Carbonell et al. (2013), Chen (2014), Coetzee et al. (2005), Cuéllar et al. (2009), Dang and Meguid (2013), Dufour et al. (2001), Gabrieli et al. (2009), Holmes et al. (2011), Hu et al. (2015), Jassim et al. (2012), Jiang and Yin (2012), Kardani et al. (2017), Khoshghalb and Khalili (2012, 2013, 2015), Komoróczi et al. (2013), Kuhnert and Ostermann (2014), Lim and Andrade (2014), Michel and Kuhnert (2015), Michel et al. (2017), Murakami et al. (2005), Obermayr et al. (2013), Obermayr and Vrettos (2013), Oñate et al. (2011a, b), Ostermann et al. (2013), Pastor et al. (2008), Peng et al. (2015), Polymerou (2017), Schenkengel and Vrettos (2011), Schneider-Muntau et al. (2017), Sloan et al. (2016), Soga et al. (2015), Tootoonchi et al. (2016), Uhlmann et al. (2013), Vermeer et al. (2008), Wu et al. (2001), and Zhu et al. (2006).

In the first part of this contribution, Ostermann et al. (2013), we discussed the application of two GFDMs to model standard benchmark problems in soil mechanics (oedometric and triaxial test). Both methods integrate the rate-independent barodesy model of Kolymbas (2011, 2012), which describes anelastic soil behavior. The previous theoretical considerations are completed by numerical results presented here. Both the Finite Pointset Method (FPM) and the Soft PARticle Code (SPARC) use an implicit approach to solve the occurring partial differential equations on a finite set of numerical points.[1] The points move according to the velocity of the continuum in a Lagrangian framework. In FPM, the nonlinear barodesy model is integrated into the standard coupled velocity-pressure formulation by local linearization resulting in a large, sparse linear system of equations which is solved by a BiCGStab(2) algorithm. The condition number of the linear system strongly depends on the number of FPM points. If necessary, regularization strategies are available. In contrast to that, SPARC directly solves the nonlinear problem by a Newton iteration scheme. Thus, SPARC exactly models the material model at the cost of solving a large, sparse nonlinear system of equations.

In addition to these basic numerical characteristics, the discretization and approximation strategies differ: (1) FPM is based on an unstructured point cloud which is continuously checked for its quality. This guarantees the applicability of the method to a large variety of problems in fluid and continuum mechanics. A moving weighted least squares procedure with polynomials up to second order is used for functional approximation on the point cloud. For details on FPM see e.g. Drumm et al. (2008), Jefferies et al. (2015), Kuhnert (2009, 2014), Kuhnert and Ostermann (2014), Michel

---

[1] Although the wording is different, points in FPM and particles in SPARC, both notations stand for numerical points without mass.

and Kuhnert (2015), Michel et al. (2017), Ostermann et al. (2013), Suchde and Kuhnert (2017), Suchde et al. (2017a, b), Tiwari and Kuhnert (2002a, b, 2004, 2005, 2007), Tiwari et al. (2007), and Tramecon and Kuhnert (2013). (2) The initial particle configuration in SPARC is regular; quality checks are not performed during a simulation. The regular character of the particle configuration reduces the number of neighbors necessary in the weighted moving least squares procedure (polynomials up to first order) considerably compared to the one in FPM. Details on SPARC can be found in Chen (2014), Polymerou (2017), and Schneider-Muntau et al. (2017).

In Sect. 2, the laboratory tests and their corresponding setups for the oedometric and the triaxial test are described. These are the basis of the following case studies for FPM and SPARC in Sects. 4 and 5, respectively. For both meshfree methods the influence of the most important parameters is analyzed with respect to quality and the ability to reproduce the rate-independent character of the barodesy model for loose and dense sand samples. The results of the respective element tests are used as reference. The necessary evaluation strategy (from 3D simulation result to stress-strain-curve etc.) is presented in Sect. 3, including the specific simulation setups for the different scenarios. The numerical results for FPM and SPARC are compared in Sect. 6, followed by conclusions in Sect. 7.

2 Laboratory tests

As described in Ostermann et al. (2013), two popular benchmark problems in soil mechanics are the oedometric and the triaxial test. The oedometric one is known as a confined compression test (see Holtz and Kovacs (1981)), which is equivalent to a homogeneous 1D compression scenario. The soil sample is loaded in axial direction and rigid side walls hinder any lateral expansion, see Fig. 1. In contrast to this, in a conventional triaxial test the soil sample is enclosed in a thin rubber membrane and placed between two plates inside a pressure chamber. The sample is then loaded in axial direction by the stress component σ_1 and by constant lateral stresses $\sigma_2 = \sigma_3$, which is denoted as confining pressure σ_c (see Fig. 2).

2.1 Oedometric test

The lab measurements for the oedometric test refer to a cylindrical sample of Hostun sand with height of 0.025 m and diameter of 0.0945 m. Details can be found in Desrues et al. (2000). In oedometric lab tests the height of the sample is minimized in order
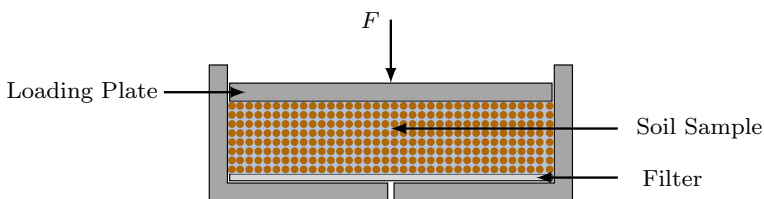
Fig. 1 Schematic illustration of the oedometric test
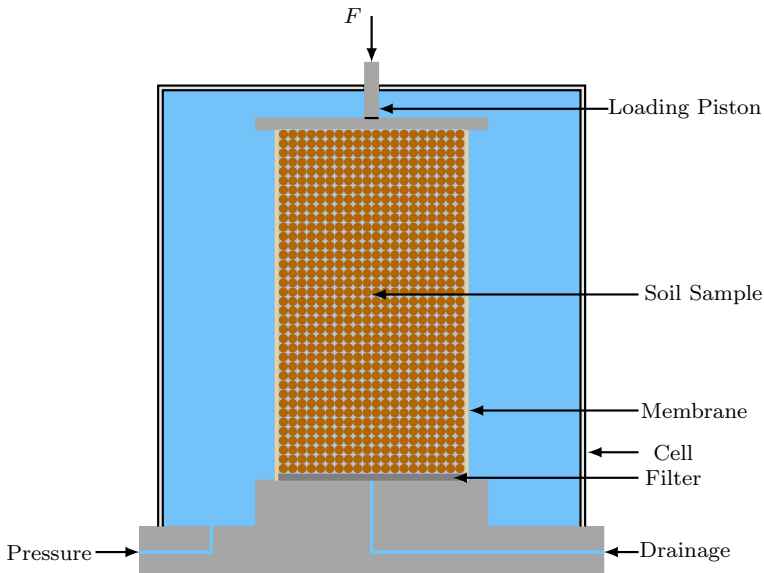
**Fig. 2** Schematic illustration of the triaxial test

Table 1 Setup for oedometric tests

	Dense sample	Loose sample
Initial void ratio	$e = 0.667$	$e = 0.8703$
Initial density	$\rho = 1590\,\text{kg/m}^3$	$\rho = 1416.9\,\text{kg/m}^3$
Loading-unloading-process (until axial strain $-\varepsilon_1$)	$0 - 0.0045 - 0.0037 - 0.0071$ $- 0.0051 - 0.0098 - 0.0062$ $- 0.0140 - 0.0077 - 0.015$	$0 - 0.01 - 0.0092 - 0.0122$ $- 0.011 - 0.0164 - 0.0138$ $- 0.0222 - 0.0175 - 0.0245$

to reduce friction effects that might spoil the measured vertical displacements. We consider both a dense and a loose setup according to Table 1. Please note that in reality oedometric tests are stress-controlled, i.e. a particular force is applied to the loading plate and the deformations are measured over the course of time. Subsequently, the strains are calculated from the recorded plate displacements. However, in our simulations the oedometric test is simulated strain-controlled referring to the loading-unloading-processes defined in Table 1 with respect to axial strain $-\varepsilon_1$. Throughout this contribution we adopt the convention of mechanics: compression is negative, tension is positive.

To predict the mechanical behavior of materials with the help of numerical schemes, we have to rely on constitutive models, such as the nonlinear barodesy model used in Ostermann et al. (2013). This rate-independent material model is given by an evolution equation for the Cauchy stress tensor $\mathbf{T} = -\boldsymbol{\sigma}$ (with principal stresses $\sigma_1, \sigma_2, \sigma_3$) in combination with an evolution equation for the void ratio e:

$$\dot{\mathbf{T}} = \mathbf{H}(\mathbf{T}, \mathbf{D}, e), \quad \dot{e} = (1 + e) \cdot \text{tr}(\mathbf{D}),$$
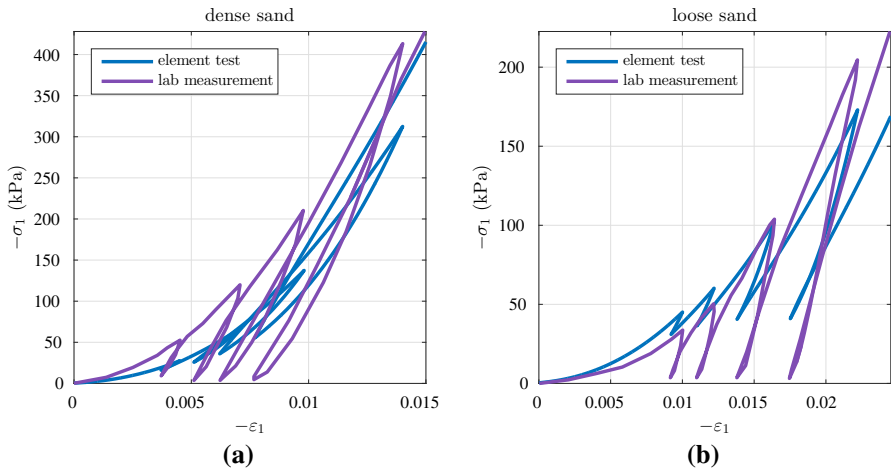
Fig. 3 *Oedometric test*—comparison of lab measurement and element test: stress-strain-curves for dense (**a**) and loose sand (**b**)

where **H** is a nonlinear tensorial function (including constants $c_1, \ldots, c_6, e_{c0}$) and **D** is the stretching tensor (i.e. the symmetric part of the velocity gradient). The material constants for Hostun sand, which is considered in the current lab measurements, are $c_1 = -1.7637$, $c_2 = -1.0249$, $c_3 = 0.5517$, $c_4 = -1174$, $c_5 = -4175$, $c_6 = 2218$, $e_{c0} = 0.8703$.

In Fig. 3, we compare the lab measurements for the chosen oedometric setup with the results obtained for the corresponding element test. In an element test the barodesy model is integrated for one numerical point with respect to the given boundary conditions. The agreement of element test and lab measurement solely depends on the quality of the constitutive model, i.e. barodesy. However, the focus of our contribution is not the analysis of the constitutive model but the quality of the considered 3D numerical schemes FPM and SPARC. Hence, the comparison of lab measurement and element test is illustrated only for the sake of completeness.

2.2 Triaxial test

For the triaxial test we proceed according to the description above. We consider a cylindrical soil sample of Hostun sand with height and diameter of 0.1 m, see Desrues et al. (2000). The setup is given in Table 2. The comparison of lab measurement and

Table 2 Setup for triaxial tests

	Dense sample	Loose sample
Initial void ratio	$e = 0.6324$	$e = 0.8442$
Initial density	$\rho = 1623.4 \,\mathrm{kg/m^3}$	$\rho = 1436.9 \,\mathrm{kg/m^3}$
Confining pressure	$-\sigma_c = 100 \,\mathrm{kPa}$	$-\sigma_c = 100 \,\mathrm{kPa}$
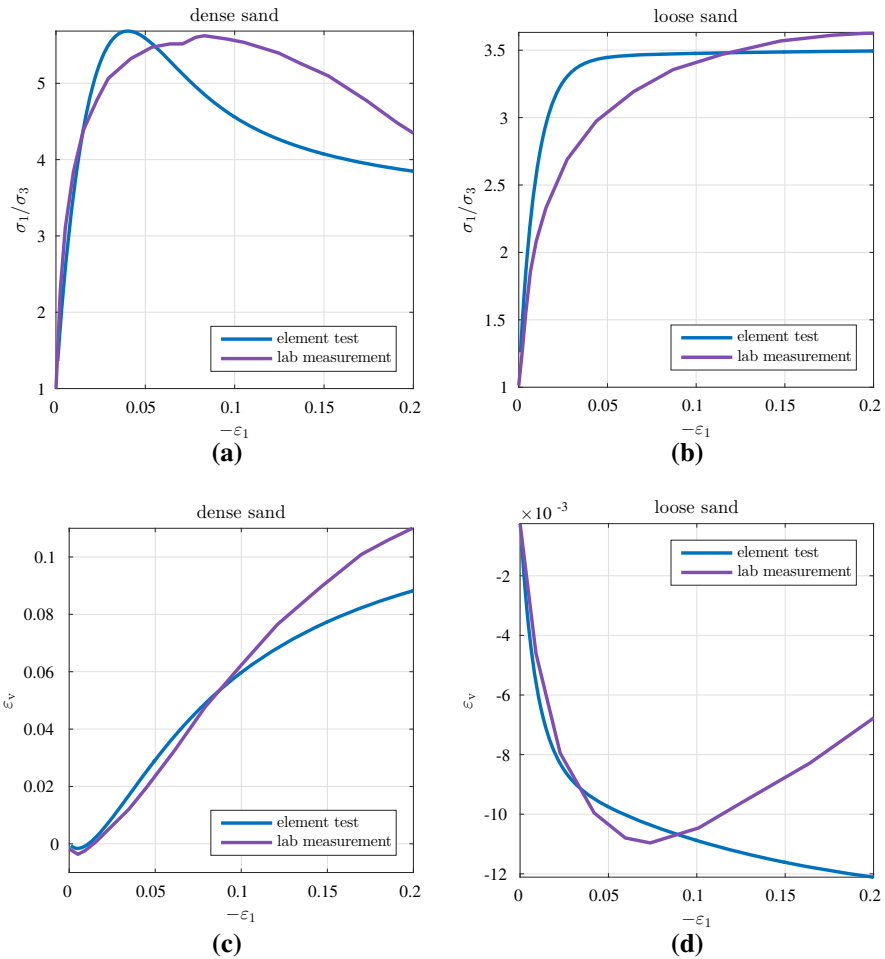
Fig. 4 *Triaxial test*—comparison of lab measurement and element test for dense (**a**, **c**) and loose sand (**b**, **d**): stress-strain-curve (first row) and volumetric-axial-strain-curve (second row)

corresponding triaxial element test can be found in Fig. 4, where the volumetric strain is given by $\varepsilon_v = \mathrm{tr}(\boldsymbol{\varepsilon})$ with strain tensor $\boldsymbol{\varepsilon}$ defined as $\dot{\boldsymbol{\varepsilon}} = \mathbf{D}$.

For both the oedometric as well as the triaxial test the element test based on the barodesy model shows a relatively good agreement with the lab measurements. However, there still is potential to enhance this constitutive model to better fit the material behavior. Specific enhancements for sand have been developed in Medicus et al. (2016) and Kolymbas (2015). For barodesy for clay see Medicus et al. (2012) and Medicus and Fellin (2017).

The aim of this contribution is to illustrate the quality of the 3D numerical schemes FPM and SPARC by realistically simulating oedometric and triaxial test scenarios for the above described setups. To this end, in Sects. 4 and 5 we compare the 3D simulation results to the respective element test since it is not the task of the numerical scheme to

fit the lab measurement but the task of the constitutive model. The numerical scheme can only be as good as the constitutive model.

3 Setup and evaluation strategy for 3D simulations

The case studies for FPM and SPARC in Sects. 4 and 5, respectively, are based on the following simulation setups independent of the test type and the sample type:

> **simulation setup I**—fixed reference loading/unloading rate, varying sample resolution (interaction radius for FPM and number of particles for SPARC)
> **simulation setup II**—fixed sample resolution, varying loading/unloading rate (based on the reference level)

In order to compare the 3D simulations to the corresponding element test, the necessary 1D stress-strain-curves and stress paths are generated by averaging the considered quantity over all points/particles at the loading plate. The volumetric-axial-strain-curves are generated by averaging over all points/particles of the simulated soil sample to accommodate the volumetric character.[2] Note that a consistent comparison of the results is guaranteed by considering the axial strain in logarithmic form. The relation between logarithmic and engineering strain is

$$\varepsilon_1^{\log} = \ln(1 + \varepsilon_1^{\mathrm{eng}}),$$

where $\varepsilon_1^{\mathrm{eng}} = $ current height/initial height (of the soil sample).

4 Case study for FPM

In this section, we present a case study for FPM for the dense and loose setups described in Tables 1 and 2. The most important parameters in the numerical scheme are analyzed: the interaction radius h, which determines the number of FPM points used to represent the soil sample; the loading/unloading rate v_p, which is coupled to the time step size Δt. We investigate the quality of the 3D FPM simulations as well as the realization of the rate-independence of the barodesy model in the numerical implementation. In case of the oedometric test, we also address the property of 1D compression.

4.1 Oedometric test

During an oedometric test the stress state is far away from the limit state, where numerical problems can occur. Since the oedometric test models homogeneous 1D compression, it is expected that a small number of FPM points is sufficient to realistically model this property. However, a natural lower limit is given by the implemented

---

[2] Averaging is absolutely necessary in case of inhomogeneous deformation occurring in the triaxial test due to friction at the plates. Homogeneous deformation does not demand for it. However, we use the described averaging strategy in both cases.

Table 3 FPM simulation parameters for the oedometric test

	Simulation setup	h (m)	v_p (m/s)	Δt (s)	$\Delta t \cdot v_p$ (m)
Dense and loose sample	I	0.02	∓ 0.001	0.0009	$\mp 9.0 \cdot 10^{-7}$
		0.01	∓ 0.001	0.0009	$\mp 9.0 \cdot 10^{-7}$
		0.005	∓ 0.001	0.0009	$\mp 9.0 \cdot 10^{-7}$
	II	0.01	∓ 0.01	0.00009	$\mp 9.0 \cdot 10^{-7}$
		0.01	∓ 0.001	0.0009	$\mp 9.0 \cdot 10^{-7}$
		0.01	∓ 0.0001	0.009	$\mp 9.0 \cdot 10^{-7}$

least squares approximation scheme for unstructured point clouds. For each FPM point 40 neighbors in the interaction radius of h are used for the functional approximation in the least squares sense.

The standard value for the loading/unloading rate in axial direction is $v_p = \mp 0.001$ m/s. Throughout this contribution this is the reference velocity. Furthermore, the initial stress state is given by

$$
\mathbf{T}(t = 0) = \begin{pmatrix} 10.0 & 0.0 & 0.0 \\ 0.0 & 10.0 \cdot K_0 & 0.0 \\ 0.0 & 0.0 & 10.0 \cdot K_0 \end{pmatrix},
$$

where $K_0 = 1 - \sin(\varphi) \approx 0.4672$ with critical friction angle $\varphi \approx 32°$. Table 3 summarizes the FPM simulation parameters for the oedometric test.

4.1.1 Dense sand

For interaction radii $h = 0.02$ m, 0.01 m, 0.005 m and fixed time step size $\Delta t = 0.0009$ s (simulation setup I) the 3D FPM simulations are compared to the element test in Fig. 5. The corresponding numbers of FPM points are about 775, 6250, and 32,600, respectively. As described in Sect. 1, the unstructured point cloud is checked regularly for its quality, especially for too large holes or accumulations. If a quality check fails, points are filled or merged as needed. Thus, the number of FPM points is not constant throughout a simulation. Choosing $h > 0.02$ m is not possible since there are not enough points for the least squares approximation. As an example, the starting point cloud configuration for interaction radius $h = 0.01$ m is illustrated in Fig. 6.

As expected, a small number of FPM points is sufficient to obtain good agreement with the element test (even in case of the coarsest point cloud resolution). Convergence with respect to the interaction radius is achieved for the medium point cloud resolution with $h = 0.01$ m. Convergence means that the result does not considerably change when further reducing the interaction radius. Consequently, 1D compression is confirmed. Thus, we now consider the medium interaction radius $h = 0.01$ m and focus on the rate-independence of the barodesy model as well as the ability of the implicit FPM solver to reproduce this property in simulation setup II. In Fig. 7, it can
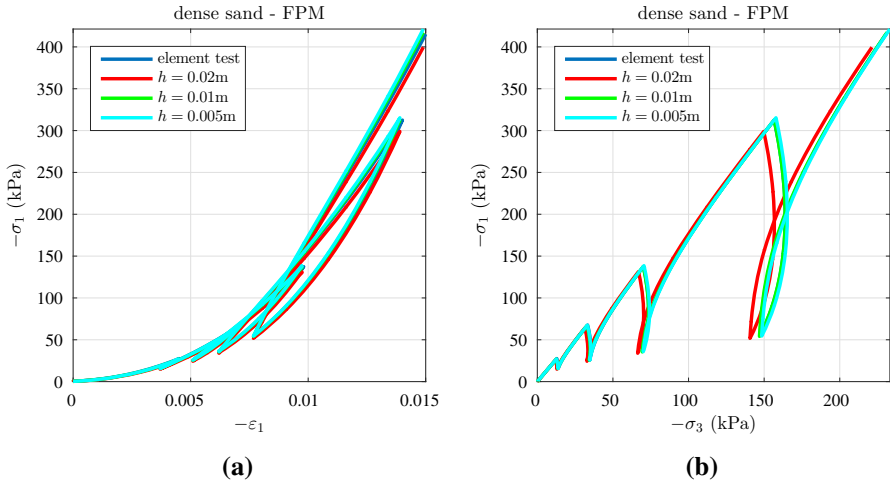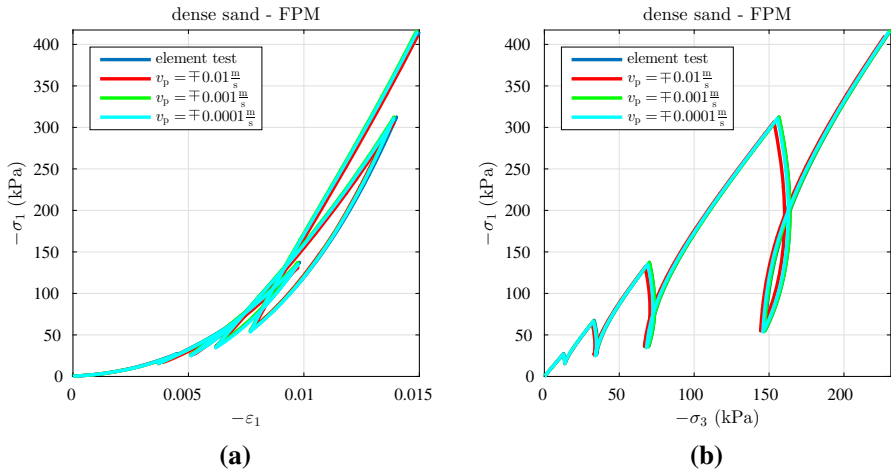
Fig. 5 *Dense oedometric test*—comparison of element test and 3D FPM simulations for simulation setup I: stress-strain-curve (**a**) and stress path (**b**)

Fig. 6 Starting FPM point cloud configuration for the oedometric test with $h = 0.01$ m (filled circles: interior points, non-filled circles: boundary points)
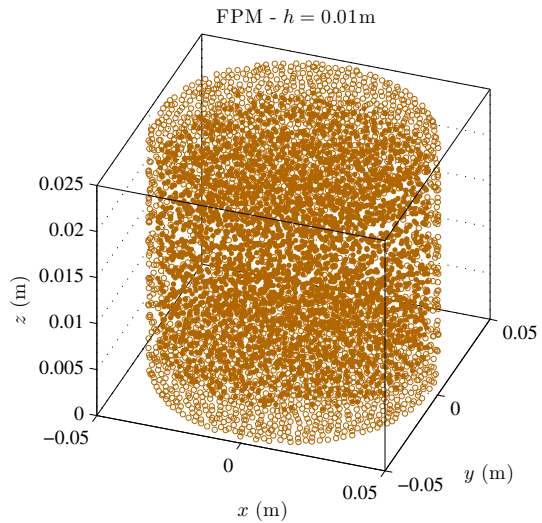

be observed that a moderate change of the axial loading/unloading rate v_p does not noticeably influence the results. A change of v_p includes a proportionate scaling of the time step size Δt, i.e. the product $\Delta t \cdot v_p$ is constant. Simulations for even larger[3] v_p show problems, especially at the transition from loading to unloading and vice versa. Nevertheless, rate-independence of barodesy can be found in a large range in the FPM implementation for the oedometric test with dense sand.

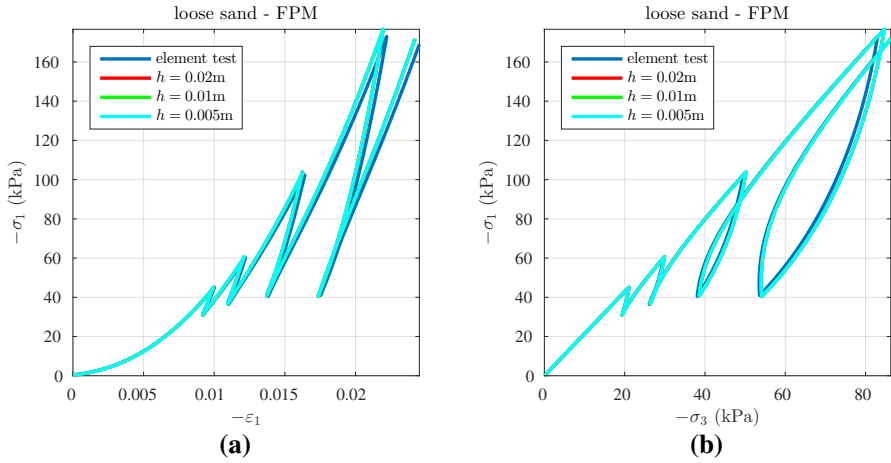
[3] In the sense of absolute value.

Fig. 7 *Dense oedometric test*—comparison of element test and 3D FPM simulations for simulation setup II: stress-strain-curve (**a**) and stress path (**b**)
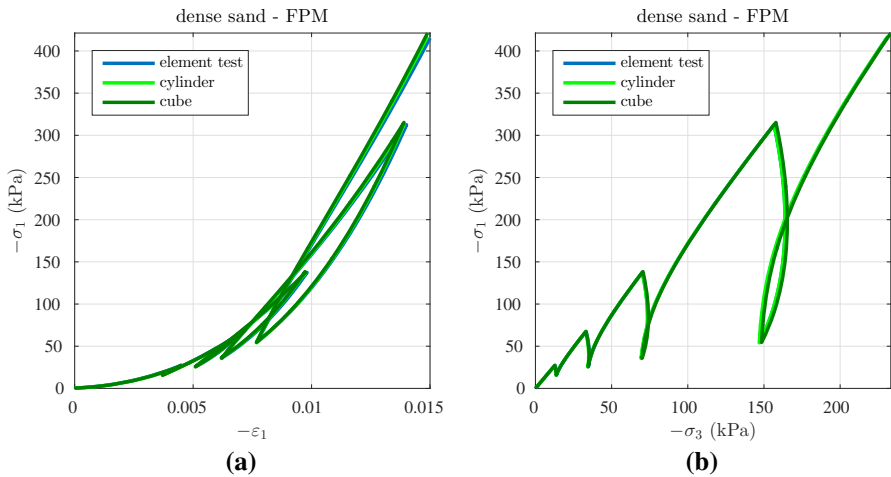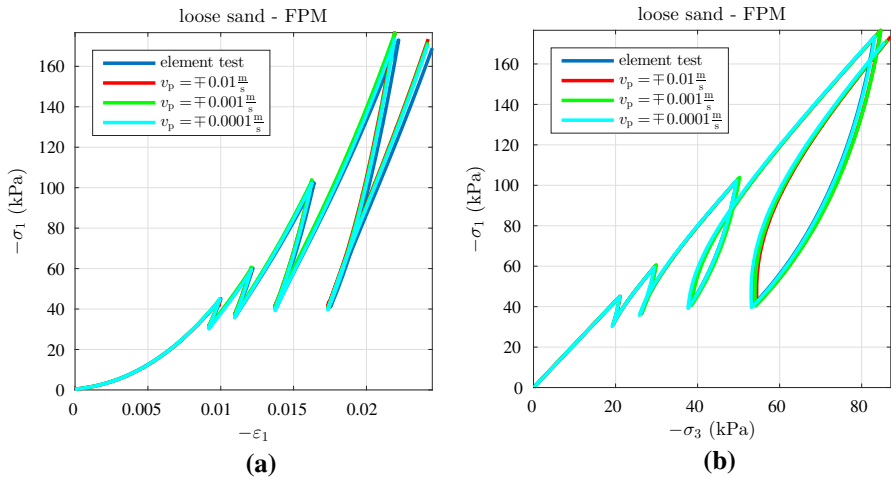

Fig. 8 *Dense oedometric test*—comparison of element test and 3D FPM simulations for different geometrical bases ($v_p = \mp 0.001$ m/s, $\Delta t = 0.0009$ s, and $h = 0.01$ m): stress-strain-curve (**a**) and stress path (**b**)

As described in Sect. 2, the geometrical basis for the above simulations is a cylinder with height of 0.025 m and diameter of 0.0945 m. The comparison of this cylindrical setup with a cubic setup (with dimensions 0.0945 m × 0.0945 m × 0.025 m) in Fig. 8 confirms that the homogeneous character of the deformation provides independence of the geometrical basis. Hence, from here on we consider the cube instead of the cylinder for the simulation of the oedometric test. For the cube the numbers of FPM points are about 1125 ($h = 0.02$ m), 7000 ($h = 0.01$ m), and 42,750 ($h = 0.005$ m).

Fig. 9 *Loose oedometric test*—comparison of element test and 3D FPM simulations for simulation setup I: stress-strain-curve (**a**) and stress path (**b**)

Fig. 10 *Loose oedometric test*—comparison of element test and 3D FPM simulations for simulation setup II: stress-strain-curve (**a**) and stress path (**b**)

4.1.2 Loose sand

The agreement of element test and 3D FPM simulations is similarly well for loose sand as for dense sand (see Fig. 9). As before, the results depend on the interaction radius h. Convergence is already achieved for the coarsest point cloud resolution, i.e. $h = 0.02$ m. Again, rate-independence can be found in a large range in the FPM implementation of the barodesy model (see Fig. 10).

In summary, FPM is able to reproduce the homogeneous character of the oedometric test for both the dense as well as the loose setup. Furthermore, rate-independence

is verified under the constraint that the product $\Delta t \cdot v_p$ of time step size and loading/unloading rate is constant. Finally, it can be observed that the time step size is independent of the setup (dense or loose).

4.2 Triaxial test

In a triaxial test, the axial stress σ_1 on the soil sample is increased until a limit state is reached. The stress-strain-curve of a dense sample is characterized by a stress peak which is followed by a softening regime, whereas in case of loose samples an asymptotical behavior is observed. Regarding the volume, dense samples are subject to dilatant effects (increasing volume under shear) while loose samples are subject to contractant effects (decreasing volume under shear). The analysis of the 3D FPM simulations is focused on the comparison with the corresponding element test as well as the realization of the rate-independence of the barodesy model.

Compared to the oedometric test, the boundary conditions in a triaxial test are more complex, especially at the free surface/membrane which is loaded by the confining pressure $-\sigma_c$. The current numerical implementation of this boundary condition in FPM is prone to oscillations which can be damped by increasing the point cloud resolution (smaller h). Reducing the interaction radius h also results in smaller time step sizes. The assumption of frictionless upper and bottom plate described in Ostermann et al. (2013) is lessened to a combination of slip and no-slip velocity condition (*constrained* triaxial test). Thereby, the center of the sample at both plates (up to 50% of the initial diameter of the sample) is subject to a no-slip velocity condition while the outer part is subject to a classical slip velocity condition. In lab tests as well as the 3D FPM simulations, this prevents horizontal sliding of the sample during loading. A more detailed discussion of this effect can be found in Sect. 5.2, where the constraining strategy in SPARC is described.

For both simulation setup I and II the FPM simulation parameters for the triaxial test can be found in Table 4. The reference loading rate is $v_p = -0.001\,\text{m/s}$ and the initial stress state is given by

$$\mathbf{T}(t=0) = \begin{pmatrix} -\sigma_c & 0.0 & 0.0 \\ 0.0 & -\sigma_c & 0.0 \\ 0.0 & 0.0 & -\sigma_c \end{pmatrix}, \quad -\sigma_c = 100\,\text{kPa}.$$

As for the oedometric test, three point cloud resolutions are considered for the reference loading rate until convergence with respect to the interaction radius is achieved. The respective resolution is then the basis for further simulations with varying loading rate. The numbers of FPM points are about 900 ($h = 0.03\,\text{m}$), 5800 ($h = 0.015\,\text{m}$), and 36,500 ($h = 0.0075\,\text{m}$).

4.2.1 Dense sand

The results for simulation setup I in Fig. 11 indicate that the quality of the 3D FPM simulations strongly depends on the chosen interaction radius h. Convergence with

Table 4 FPM simulation parameters for the triaxial test

|	Simulation setup	h (m)	v_p (m/s)	Δt (s)	$\Delta t \cdot v_p$ (m)
Dense sample	I	0.03	-0.001	0.015	$-1.5 \cdot 10^{-5}$
		0.015	-0.001	0.01	$-1.0 \cdot 10^{-5}$
		0.0075	-0.001	0.005	$-5.0 \cdot 10^{-6}$
	II	0.0075	-0.01	0.0005	$-5.0 \cdot 10^{-6}$
		0.0075	-0.001	0.005	$-5.0 \cdot 10^{-6}$
		0.0075	-0.0001	0.05	$-5.0 \cdot 10^{-6}$
Loose sample	I	0.03	-0.001	0.01	$-1.0 \cdot 10^{-5}$
		0.015	-0.001	0.01	$-1.0 \cdot 10^{-5}$
		0.0075	-0.001	0.005	$-5.0 \cdot 10^{-6}$
	II	0.0075	-0.01	0.0005	$-5.0 \cdot 10^{-6}$
		0.0075	-0.001	0.005	$-5.0 \cdot 10^{-6}$
		0.0075	-0.0001	0.05	$-5.0 \cdot 10^{-6}$

(a)

(b)
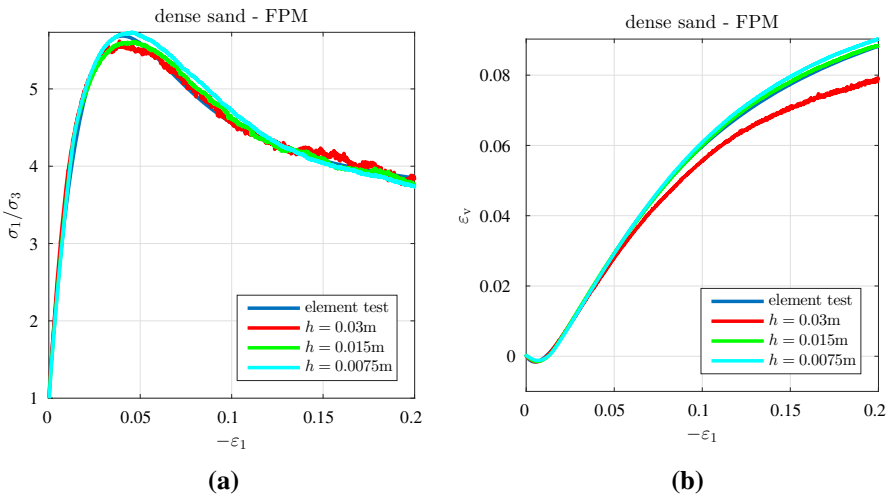
Fig. 11 *Dense triaxial test*—comparison of element test and 3D FPM simulations for simulation setup I: stress-strain-curve (**a**) and volumetric-axial-strain-curve (**b**)

respect to h and, thus, a good agreement with the element test is achieved only for the high resolution with $h = 0.0075$ m. This is due to the implemented local linearization and the adaption of the confining pressure boundary condition at the free surface. Furthermore, point cloud refinement also necessitates a decrease in the time step size contrary to the observations for the oedometric test. The smallest interaction radius is the basis for simulation setup II, see Fig. 12. As for the oedometric test, rate-independence of barodesy can be found in a large range if the time step size is adapted properly ($\Delta t \cdot v_p$ constant).
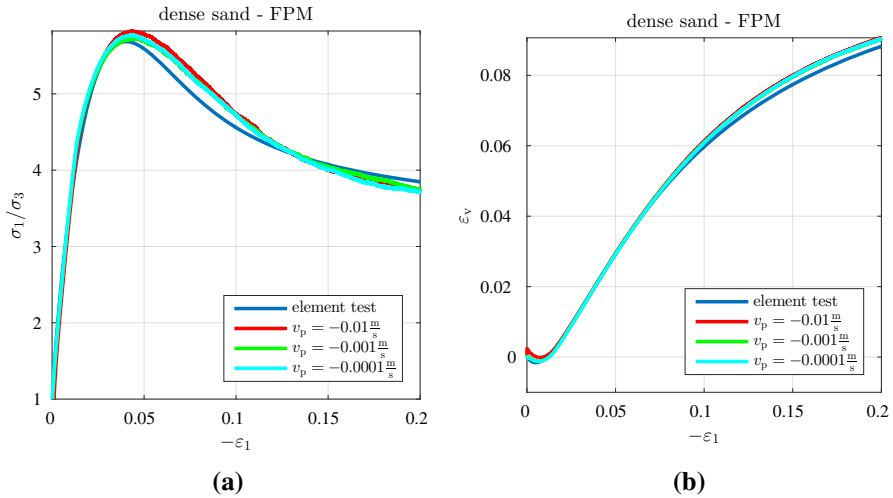
Fig. 12 *Dense triaxial test*—comparison of element test and 3D FPM simulations for simulation setup II: stress-strain-curve (**a**) and volumetric-axial-strain-curve (**b**)
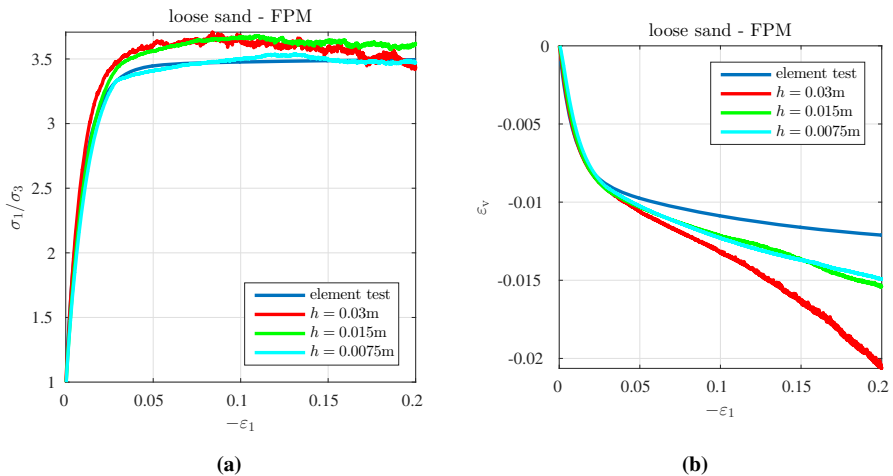
Fig. 13 *Loose triaxial test*—comparison of element test and 3D FPM simulations for simulation setup I: stress-strain-curve (**a**) and volumetric-axial-strain-curve (**b**)

4.2.2 Loose sand

The results for loose sand are similar to the ones for dense sand even though slightly larger deviations can be observed, especially for the volumetric strain. Convergence with respect to the interaction radius is achieved for $h = 0.0075$ m with adapted time step size (see Fig. 13). Furthermore, rate-independence is confirmed in Fig. 14.

The numerical analysis of the triaxial test shows that FPM is able to capture dilatant (dense sand) as well as contractant (loose sand) effects under different loading regimes.
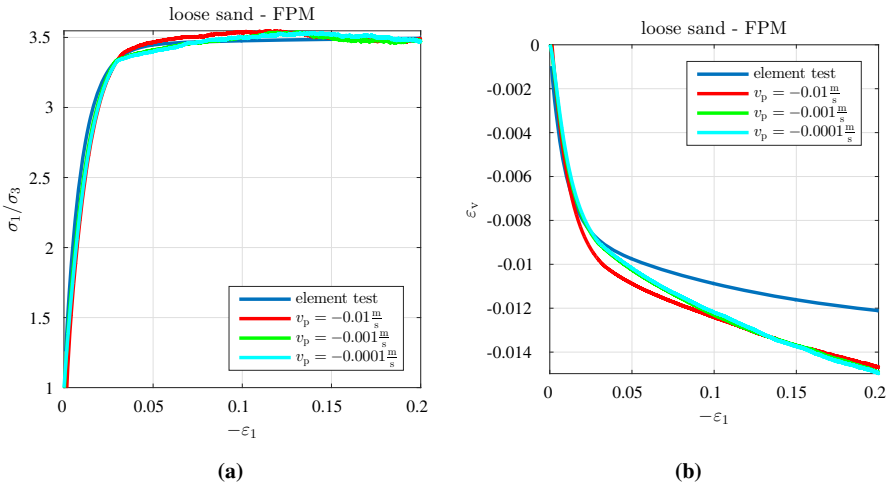
Fig. 14 *Loose triaxial test*—comparison of element test and 3D FPM simulations for simulation setup II: stress-strain-curve (**a**) and volumetric-axial-strain-curve (**b**)

However, there is still potential to stabilize the local linearization scheme with respect to the point cloud resolution. This is essential to reliably simulate real life applications.

5 Case study for SPARC

In this section, we present a case study for SPARC according to the one for FPM in Sect. 4. Again, the most important parameters in the numerical scheme are analyzed: these are the number of particles p to represent the soil sample and the loading/unloading rate v_p. In contrast to FPM, SPARC does not add or remove particles, although this is in principle possible. Therefore, the number of particles remains constant throughout a simulation.
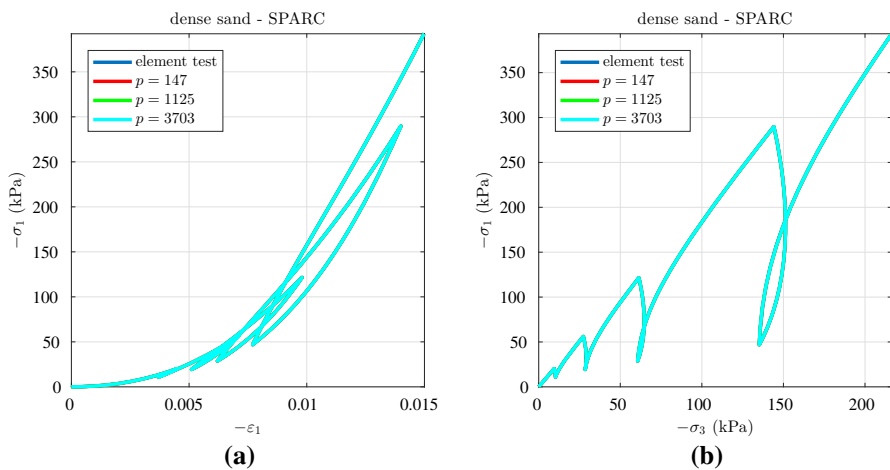
5.1 Oedometric test

In Table 5, the SPARC simulation parameters for the oedometric test are summarized. For both the dense and the loose sample we consider the reference loading/unloading rate $v_p = \mp 0.001$ m/s and three different numbers of particles (simulation setup I). Furthermore, simulations for the medium number of particles $p = 1125$ and three different loading/unloading rates are analyzed (simulation setup II). Due to the applied boundary conditions and the homogeneous deformation, convergence of the Newton iteration scheme to solve the nonlinear system of equations is achieved relatively easy.

5.1.1 Dense sand

The 3D SPARC simulations for simulation setup I show excellent agreement with the element test, see Fig. 15. Since the deformation is homogeneous, the number

Table 5 SPARC simulation parameters for the oedometric test

|	Simulation setup	p	v_p (m/s)	Δt (s)	$\Delta t \cdot v_\mathrm{p}$ (m)
Dense sample	I	147	∓ 0.001	0.0025	$\mp 2.5 \cdot 10^{-6}$
		1125	∓ 0.001	0.0025	$\mp 2.5 \cdot 10^{-6}$
		3703	∓ 0.001	0.0025	$\mp 2.5 \cdot 10^{-6}$
	II	1125	∓ 0.01	0.0025	$\mp 2.5 \cdot 10^{-5}$
		1125	∓ 0.001	0.0025	$\mp 2.5 \cdot 10^{-6}$
		1125	∓ 0.0001	0.0025	$\mp 2.5 \cdot 10^{-7}$
Loose sample	I	147	∓ 0.001	0.0025	$\mp 2.5 \cdot 10^{-6}$
		1125	∓ 0.001	0.0025	$\mp 2.5 \cdot 10^{-6}$
		3703	∓ 0.001	0.0025	$\mp 2.5 \cdot 10^{-6}$
	II	1125	∓ 0.01	0.001	$\mp 1.0 \cdot 10^{-5}$
		1125	∓ 0.001	0.001	$\mp 1.0 \cdot 10^{-6}$
		1125	∓ 0.0001	0.001	$\mp 1.0 \cdot 10^{-7}$

Fig. 15 *Dense oedometric test*—comparison of element test and 3D SPARC simulations for simulation setup I: stress-strain-curve (**a**) and stress path (**b**)

of particles has no influence on the accuracy. Therefore, the curves for the different resolutions almost perfectly fit to the curve of the element test.

The results for simulation setup II are illustrated in Fig. 16. Only in case of loading/unloading rate $v_\mathrm{p} = \mp 0.01$ m/s a slight deviation from the element test can be observed. This is due to the fact that the time step size Δt is kept constant for all v_p. Adapting the time step size such that the product $\Delta t \cdot v_\mathrm{p}$ is constant would lead to an even better agreement for $v_\mathrm{p} = \mp 0.01$ m/s.
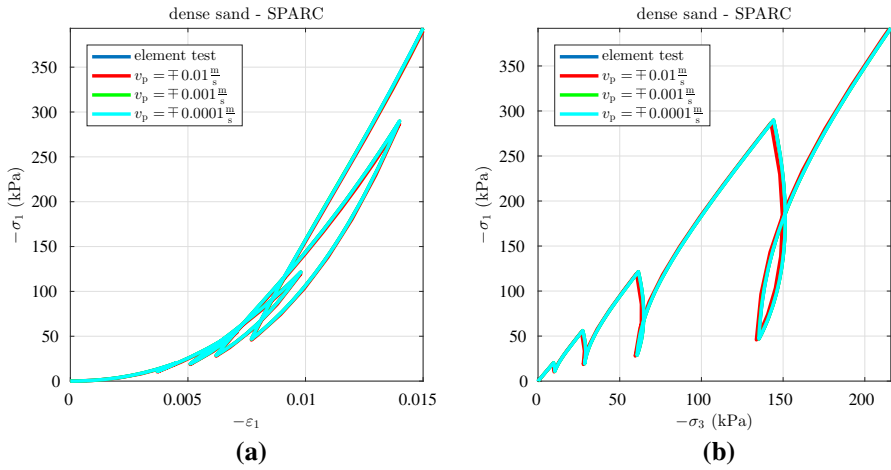
Fig. 16 *Dense oedometric test*—comparison of element test and 3D SPARC simulations for simulation setup II: stress-strain-curve (**a**) and stress path (**b**)
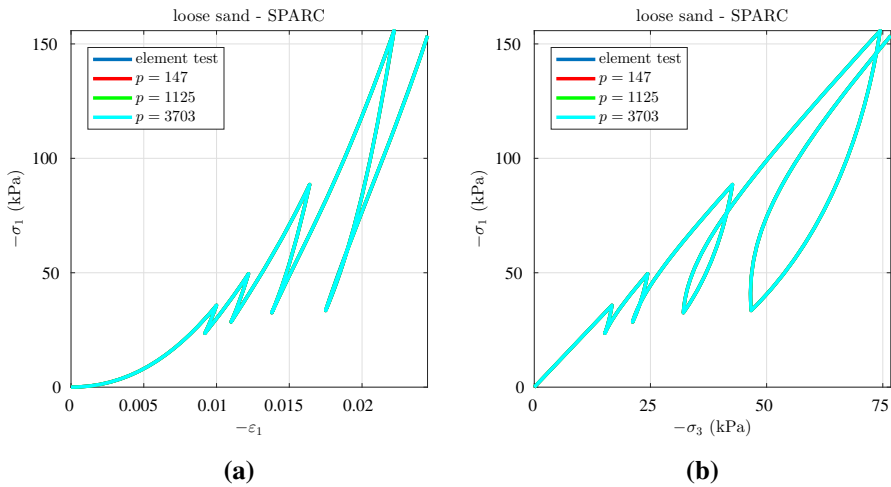
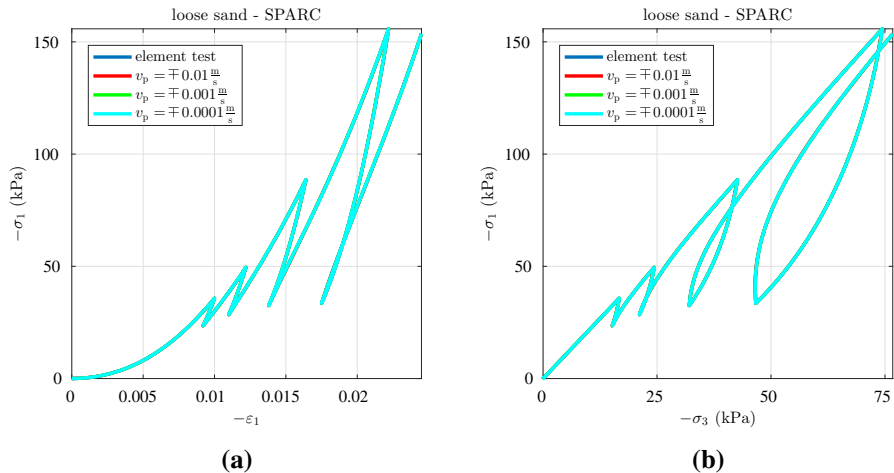**Fig. 17** *Loose oedometric test*—comparison of element test and 3D SPARC simulations for simulation setup I: stress-strain-curve (**a**) and stress path (**b**)

5.1.2 Loose sand

As before, the 3D SPARC simulations are in very good agreement with the element test for loose sand considering varying particle numbers (simulation setup I), cf. Fig. 17. However, SPARC encounters convergence difficulties for loose sand in case of $v_p = \mp 0.01$ m/s and $\Delta t = 0.0025$ s after the first unloading at axial strain $-\varepsilon_1 = 0.01$. Due to the change from loading to unloading, the initial guess of the solution, which is inherited from the previous time step, becomes an inadequate choice. In order to guarantee convergence of the Newton solver, Δt is incrementally reduced until

Fig. 18 *Loose oedometric test*—comparison of element test and 3D SPARC simulations for simulation setup II: stress-strain-curve (**a**) and stress path (**b**)

convergence is achieved with $\Delta t = 0.001$ s. This value is used for all three simulations with varying v_p, i.e. simulation setup II (see Fig. 18).
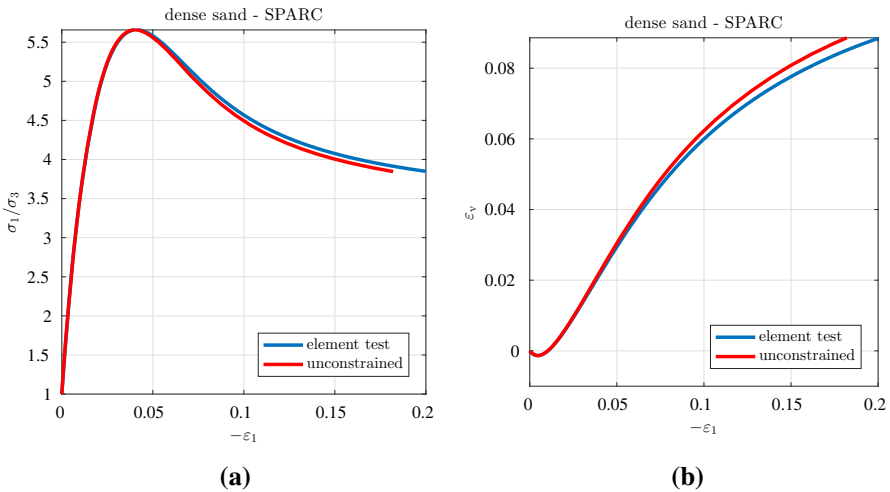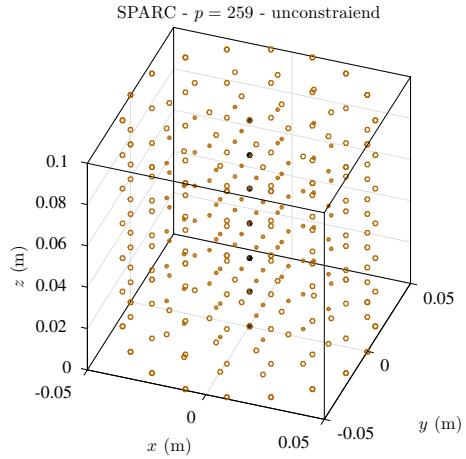
5.2 Triaxial test

The triaxial test is characterized by specific boundary conditions: fixed vertical velocity at the plate and fixed confining pressure at the membrane. This makes convergence of the Newton iteration scheme difficult or sometimes even impossible. Consequently, SPARC is very sensitive to the number of particles p, the loading rate v_p, and the time step size Δt.

Another important factor is the mode of constraint of particles in x- and y-directions. To illustrate the influence of this factor, we consider a dense sample where the particles located on the symmetry line are set free to move in x- and y-directions (see Fig. 19). The results of this *unconstrained* simulation can be found in Fig. 20. However, the inherent assumption of frictionless plates does not necessarily correspond to reality. Usually, filter stones with rough surfaces are located at the center of the sample on both plates to prevent the sample from sliding horizontally during the experiment (even if the plates are lubricated). The high degree of freedom results in severe convergence problems in the Newton solver even before the localization of deformation.[4] This ultimately leads to the abortion of the simulation at maximum axial strain of $-\varepsilon_1 = 0.18$. Therefore, for the following SPARC simulations the motion of particles located on the symmetry line is constrained in x- and y-direction,

---

[4] Localization of deformation means that with increasing loading the deformation of a solid body localizes in narrow zones which gradually develops to shear bands. This occurs when the stiffness approaches zero. Vanishing stiffness leads to an ill-posed initial boundary value problem inducing convergence problems in the Newton solver. For further details see Schneider-Muntau et al. (2017).

Fig. 19 Starting SPARC
particle configuration for the
triaxial test with $p = 259$ (filled
circles: interior particles,
non-filled circles: boundary
particles). The black,
unconstrained particles are
located on the symmetry line

Fig. 20 Comparison of element test and 3D SPARC simulation for the *unconstrained* triaxial test with dense sand ($p = 259$, $v_\mathrm{p} = -0.01$ m/s, and $\Delta t = 0.01$ s): stress-strain-curve (**a**) and volumetric-axial-strain-curve (**b**)

while the other particles are set free to move in all directions. Due to the differing discretization strategies in SPARC and FPM, the constraining strategies are also different (cf. Sect. 4.2).

The SPARC simulation parameters for the triaxial test are summarized in Table 6, where $(-\varepsilon_1)_\mathrm{max}$ denotes the maximum axial strain reached during the respective simulation. Again, for both the dense and the loose sample simulations with reference loading rate $v_\mathrm{p} = -0.001$ m/s and three different numbers of particles are considered (simulation setup I). Moreover, rate-independence is investigated in simulation setup II.

Table 6 SPARC simulation parameters for the triaxial test

	Simulation setup	p	v_{p} (m/s)	Δt (s)	$\Delta t \cdot v_{\mathrm{p}}$ (m)	$(-\varepsilon_1)_{\max}$
Dense sample	I	222	−0.001	0.4	$-4.0 \cdot 10^{-4}$	0.2
		441	−0.001	0.4	$-4.0 \cdot 10^{-4}$	0.16
		567	−0.001	0.4	$-4.0 \cdot 10^{-4}$	0.11
	II	441	−0.01	0.06	$-6.0 \cdot 10^{-4}$	0.08
		441	−0.001	0.06	$-6.0 \cdot 10^{-5}$	0.05
		441	−0.0001	0.06	$-6.0 \cdot 10^{-6}$	0.02
Loose sample	I	222	−0.001	0.4	$-4.0 \cdot 10^{-4}$	0.2
		441	−0.001	0.4	$-4.0 \cdot 10^{-4}$	0.12
		567	−0.001	0.4	$-4.0 \cdot 10^{-4}$	0.05
	II	441	−0.01	0.05	$-5.0 \cdot 10^{-4}$	0.10
		441	−0.001	0.05	$-5.0 \cdot 10^{-5}$	0.10
		441	−0.0001	0.05	$-5.0 \cdot 10^{-6}$	0.01

(a)

(b)
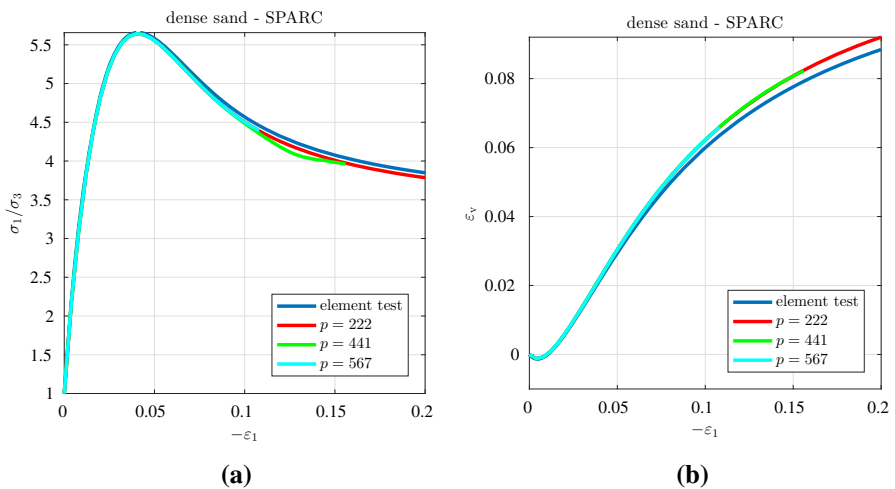
Fig. 21 *Dense triaxial test*—comparison of element test and 3D SPARC simulations for simulation setup I: stress-strain-curve (**a**) and volumetric-axial-strain-curve (**b**)

5.2.1 Dense sand

The illustration of the results for simulation setup I in Fig. 21 reveals that the larger the number of particles is, the earlier SPARC encounters convergence problems. Obviously, nonlinear problems with higher degrees of freedom involving the described, specific boundary conditions are more difficult to be solved by the Newton solver than problems with lower degrees of freedom. In general, good agreement with the element test is achieved before the stress peak. Minor deviations can be observed after the peak.
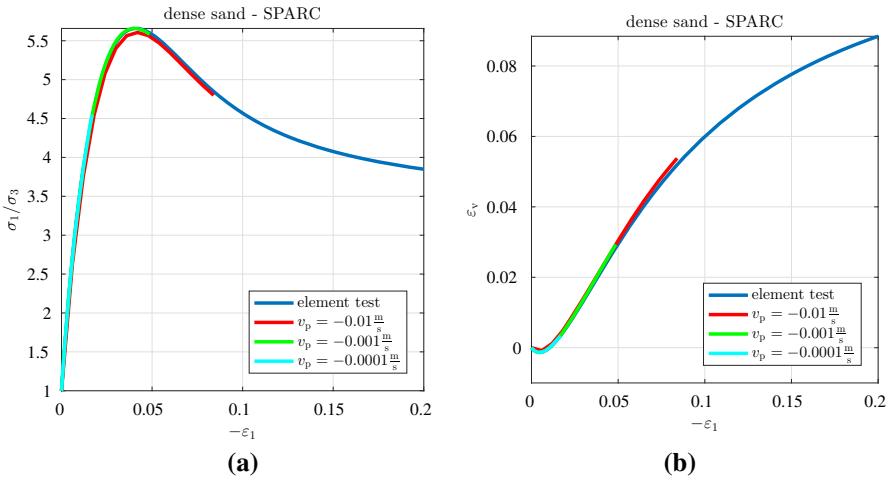
Fig. 22 *Dense triaxial test*—comparison of element test and 3D SPARC simulations for simulation setup II: stress-strain-curve (**a**) and volumetric-strain-curve (**b**)

Severe convergence problems are already encountered in the first time step in case of $v_\mathrm{p} = -0.01$ m/s and $\Delta t = 0.4$ s. Therefore, Δt is incrementally reduced to $\Delta t = 0.06$ s until convergence is achieved. In Fig. 22, the results for simulation setup II are presented. It is obvious that the smaller[3] the loading rate is, the earlier SPARC diverges: For $v_\mathrm{p} = -0.001$ m/s SPARC diverges right after the stress peak, whereas for $v_\mathrm{p} = -0.0001$ m/s even the peak of the stress-strain-curve is not reached. In case of small loading rates the numerical errors accumulate to such an extent that convergence of the Newton solver is difficult or even impossible.

5.2.2 Loose sand

The results for loose sand with simulation setup I are illustrated in Fig. 23. As for the dense sample, the larger the number of particles is, the earlier SPARC encounters convergence problems. Again, this happens due to higher degrees of freedom. Nevertheless, the 3D SPARC simulations agree well with the element test before and slightly after the plateau of the stress-strain-curve.

As before, for the highest[3] loading rate $v_\mathrm{p} = -0.01$ m/s convergence problems can be observed for large time step sizes. Therefore, Δt is incrementally reduced to $\Delta t = 0.05$ s until convergence is achieved for simulation setup II. Figure 24 shows that the smaller[3] the loading rate is, the earlier SPARC diverges. For $v_\mathrm{p} = -0.01$ m/s, -0.001 m/s SPARC diverges at almost $-\varepsilon_1 = 0.1$. For $v_\mathrm{p} = -0.0001$ m/s even the plateau of the stress-strain-curve is not reached. This is again due to the accumulation of numerical errors for small loading rates v_p.

6 Comparison of FPM and SPARC

The discretization strategies in FPM and SPARC are pretty different: On the one hand, FPM is based on an unstructured point cloud which is continuously checked for its
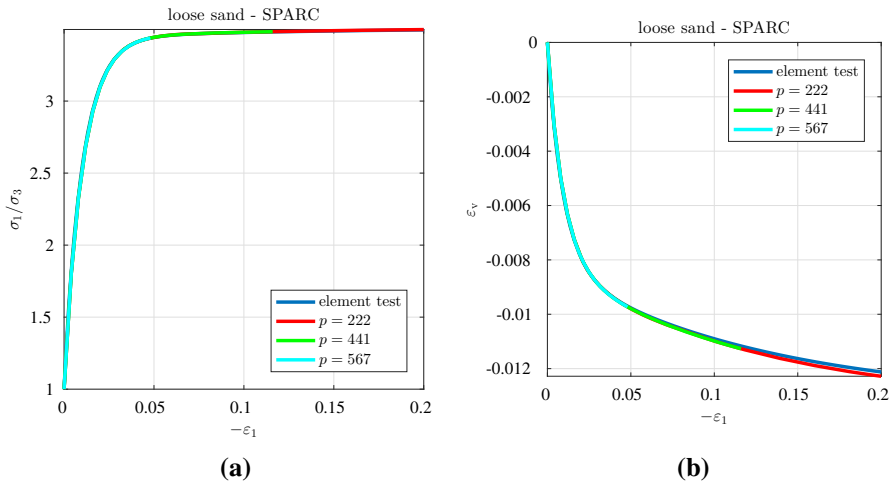
Fig. 23 *Loose triaxial test*—comparison of element test and 3D SPARC simulations for simulation setup I: stress-strain-curve (**a**) and volumetric-axial-strain-curve (**b**)
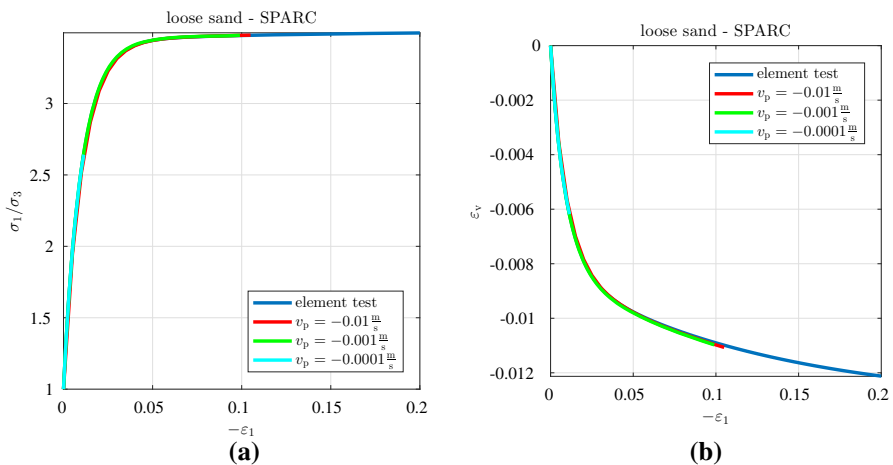
Fig. 24 *Loose triaxial test*—comparison of element test and 3D SPARC simulations for simulation setup II: stress-strain-curve (**a**) and volumetric-axial-strain-curve (**b**)

quality. Holes are filled and accumulations of points are dissolved by clustering. On the other hand, the initial distribution of particles in SPARC is regular. Furthermore, there is no adding and removing of particles throughout a simulation. Due to the unstructured character of the FPM point cloud, more neighbors are necessary for functional approximation in a weighted moving least squares scheme as described in Ostermann et al. (2013). This accounts for the larger number of points which have to be used in FPM to reproduce the element tests and the rate-independence of the nonlinear barodesy model for the oedometric as well as the triaxial test. The larger number of points is attended by smaller time step sizes.

As long as the product $\Delta t \cdot v_\mathrm{p}$ of time step size and loading/unloading rate is small enough, the 3D SPARC simulations match very well with the element tests and show no oscillations regardless of the number of particles. However, the convergence of the Newton iteration scheme, which is used to directly solve the nonlinear barodesy model, is pretty sensitive to the initial guess. This can be clearly observed for the triaxial test which is characterized by a high degree of freedom, especially in case of large numbers of particles p and small loading rate v_p.

For FPM the triaxial test is also more challenging than the oedometric test. Due to the local linearization approach, which is used to integrate the nonlinear barodesy model into the standard coupled velocity-pressure formulation, oscillations occur for coarse point cloud resolutions. But they can be damped to a certain extent by increasing the resolution, i.e. decreasing the interaction radius h. Unlike the behavior in SPARC, the adequate choice of the time step size Δt allows for high quality simulations without abortion.

We intentionally omit the explicit comparison of FPM and SPARC regarding runtime due to the following reasons: (1) Different hardware was used for the simulations. (2) FPM and SPARC are implemented in different programming languages, namely Fortran 90/95 and MATLAB, respectively. (3) FPM has been under development for a much longer time than SPARC. As a result, the implementation is more efficient. Depending on the type of simulation (oedometric or triaxial test) the runtime is of the order of several minutes to a few hours for both methods.

7 Conclusion

The theoretical description of the meshfree generalized finite difference methods FPM and SPARC in Ostermann et al. (2013) is completed in this contribution. We presented numerical case studies for the oedometric and the triaxial test with respect to the critical parameters, namely the interaction radius h (FPM)/number of particles p (SPARC), the loading/unloading rate v_p, and the time step size Δt.

The differences of the FPM and SPARC simulation results regarding spatial resolution, quality, and stability reflect the different numerical approaches as well as discretization strategies. The implicit approach implemented in FPM, which includes a local linearization of the barodesy model to comply with its standard formulation, proves to be more stable than the implicit and fully nonlinear ansatz used in SPARC. However, this comes with a price tag in terms of higher point cloud resolution and smaller time step sizes to guarantee accuracy and rate-independence of the numerical scheme.

In combination with the implementation of the confining pressure condition at the free surface of the soil sample, the local linearization leads to oscillations in the 3D FPM simulations for the triaxial test. Damping of the oscillations is possible by decreasing the interaction radius. The high quality of the results for both the oedometric as well as the triaxial test is based on the least squares approximation using up to second order polynomials on an unstructured point cloud. Currently, we investigate the sensitivity of FPM relating to the time step size in more detail.

As long as deformations are homogeneous, the 3D SPARC simulations are in excellent agreement with the element test. Although the Newton solver suffers from convergence problems, especially in the softening regime, SPARC is capable of modeling triaxial tests beyond the stress peak. In contrast to FPM, it uses a least squares approximation based on first order polynomials and a regular initial particle distribution. Chen (2014) has shown that the Newton iteration method and the Levenberg–Marquardt method encounter convergence problems close to the stress peak; even the arc-length methods cannot find a solution when deformation becomes large. This behavior is related to the fact that the physical problem becomes ill-posed. Adequate regularization techniques are currently analyzed. Since the Broyden–Fletcher–Goldfarb–Shanno (BFGS) algorithm has proven to work well in finite element methods for such problems (see Bathe 2014 and the references therein), this could be an alternative to the classical Newton solver.

In conclusion, both meshfree methods can successfully model large deformations for quasi-static problems. Future research is focused on expanding the range of application to dynamic processes as well as processes which are characterized by temporally or spatially separated quasi-static and dynamic behavior. First attempts for FPM have been made in Michel et al. (2017).

References

Abe, K., Nakamura, S., Nakamura, H., Shiomi, K.: Numerical study on dynamic behavior of slope models including weak layers from deformation to failure using material point method. Soils Found **57**(2), 155–175 (2017)

Bandara, S., Soga, K.: Coupling of soil deformation and pore fluid flow using material point method. Comput. Geotech. **63**, 199–214 (2015)

Bardenhagen, S.G., Brackbill, J.U., Sulsky, D.: The material-point method for granular materials. Comput. Methods Appl. Mech. Eng. **187**, 529–541 (2000)

Bathe, K.-J.: Finite Element Procedures, 2nd edn. Bathe K-J, Watertown (2014). ISBN 978-0-9790049-5-7

Beuth, L., Więckowski, L., Vermeer, P.A.: Solution of quasi-static large-strain problems by the material point method. Int. J. Numer. Anal. Methods Geomech. **35**, 1451–1465 (2011)

Beuth, L., Ceccato, F., Rohe, A.: Modelling of cone penetration testing with the matrial point method. Bemessen mit numerischen Methoden, Workshop 24./25.09.2013, TU Hamburg-Harburg, pp. 8–25 (2013)

Bhandari, T., Hamad, F., Moormann, C., Sharma, K.G., Westrich, B.: Numerical modelling of seismic slope failure using MPM. Comput. Geotech. **75**, 126–134 (2016)

Blanc T (2008) Numerical simulation of debris flows with the 2D-SPH depth integrated model. Master Thesis, Institute for Mountain Risk Engineering, University of Natural Resources and Applied Life Sciences, Vienna

Blanc, T., Pastor, M.: A stabilized smoothed particle hydrodynamics, Taylor–Galerkin algorithm for soil dynamics problems. Int. J. Numer. Anal. Methods Geomech. **37**, 1–30 (2013)

Bui, H.H., Fukagawa, R.: An improved SPH method for saturated soils and its application to investigate the mechanisms of embankment failure: case of hydrostatic pore-water pressure. Int. J. Numer. Anal. Methods Geomech. (2011). doi:10.1002/nag.1084

Bui, H.H., Kodikara, J.A., Pathegama, R., Bouazza, A., Haque, A.: Large deformation and post-failure simulations of segmental retaining walls using mesh-free method (SPH). CoRR (2015). arxiv:1501.04000

Carbonell, J.M., Oñate, E., Suárez, B.: Modelling of tunnelling processes and rock cutting tool wear with the particle finite element method. Comput. Mech. **52**(3), 607–629 (2013)

Chen, C.-H.: Development of Soft Particle Code (SPARC). Ph.D. Thesis, University of Innsbruck, Logos Verlag Berlin GmbH (2014)

Chen, J.-S., Hillman, M., Chi, S.-W.: Meshfree methods: progress made after 20 years. J. Eng. Mech. **143**(4), 04017001 (2017)

Coetzee, C.J., Vermeer, P.A., Basson, A.H.: The modelling of anchors using the material point method. Int. J. Numer. Anal. Methods Geomech. **29**, 879–895 (2005)

Cuéllar, P., Baeßler, M., Rücker, W.: Ratcheting convective cells of sand grains around offshore piles under cyclic lateral loads. Granul. Matter **11**, 379–390 (2009)

Dang, H.K., Meguid, M.A.: An efficient finite-discrete element method for quasi-static nonlinear soil–structure interaction problems. Int. J. Numer. Anal. Methods Geomech. **37**(2), 130–149 (2013)

Desrues, J., Zweschper, B., Vermeer, P.A.: Database for Tests on Hostun RF Sand. Technical Report, Institute of Geotechnical Engineering, University of Stuttgart (2000)

Drumm, C., Tiwari, S., Kuhnert, J., Bart, H.J.: Finite pointset method for simulation of the liquid–liquid flow field in an extractor. Comput. Chem. Eng. **32**(12), 2946–2957 (2008)

Dufour, F., Mühlhaus, H.-B., Moresi, L.: A particle-in-cell formulation for large deformation in Cosserat continua. In: Mühlhaus, H.-B., Dyskin, A., Pasternak, E. (eds.) Bifurcation and Localization in Soils and Rocks, pp. 133–138. Balkema, Leiden (2001)

Gabrieli, F., Cola, S., Calvetti, F.: Use of an up-scaled DEM model for analysing the behavior of a shallow foundation on a model slope. Geomech. Geoeng. **4**(2), 109–122 (2009)

Holmes, D.W., Williams, J.R., Tilke, P., Leonardi, C.R.: Characterizing flow in oil reservoir rock using SPH: absolute permeability. Int. J. Numer. Anal. Methods Geomech. **61**(7), 1–6 (2011)

Holtz, R.D., Kovacs, W.D.: An Introduction to Geotechnical Engineering. Prentice Hall, Englewood Cliffs (1981)

Hu, M., Liu, M.B., Xie, M.W., Liu, G.R.: Three-dimensional run-out analysis and prediction of flow-like landslides using smoothed particle hydrodynamics. Environ. Earth Sci. **73**(4), 1629–1640 (2015)

Jassim, I., Stolle, D., Vermeer, P.: Two-phase dynamic analysis by material point method. Int. J. Numer. Anal. Methods Geomech. (2012). doi:10.1002/nag.2146

Jefferies, A., Kuhnert, J., Aschenbrenner, L., Giffhorn, U.: Finite pointset method for the simulation of a vehicle travelling through a body of water. In: Griebel, M., Schweitzer, M.A. (eds.) Meshfree Methods for Partial Differential Equations VII, pp. 205–221. Springer, Berlin (2015)

Jiang, M., Yin, Z.-Y.: Analysis of stress redistribution in soil and earth pressure on tunnel lining using discrete element method. Tunn. Undergr. Sp. Tech. **32**, 251–259 (2012)

Kardani, O., Nazem, M., Kardani, M., Sloan, S.: On the application of the maximum entropy meshfree method for elastoplastic geotechnical analysis. Comput. Geotech. **84**, 68–77 (2017)

Khoshghalb, A., Khalili, N.: A Meshfree method for fully coupled analysis of flow and deformation in unsaturated porous media. Int. J. Numer. Anal. Methods Geomech. (2012). doi:10.1002/nag.1120

Khoshghalb, A., Khalili, N.: A meshfree method for fully coupled analysis of flow and deformation in unsaturated porous media. Int. J. Numer. Anal. Methods Geomech. **37**(7), 716–743 (2013)

Khoshghalb, A., Khalili, N.: An alternative approach for quasi-static large deformation analysis of saturated porous media using meshfree method. Int. J. Numer. Anal. Methods Geomech. **39**, 913–936 (2015)

Kolymbas, D.: Barodesy: a new hypoplastic approach. Int. J. Numer. Anal. Methods Geomech. **36**, 1220–1240 (2011)

Kolymbas, D.: Barodesy: a new constitutive frame for soils. Géotech. Lett. **2**, 17–23 (2012)

Kolymbas, D.: Introduction to barodesy. Géotechnique **65**(1), 52–65 (2015). doi:10.1680/geot.14.P.151

Komoróczi, A., Abe, S., Urai, J.L.: Meshless numerical modeling of brittle-viscous deformation: first results on boudinage and hydrofracturing using a coupling of discrete element method (DEM) and smoothed particle hydrodynamics (SPH). Comput. Geosci. **17**(2), 373–390 (2013)

Kuhnert, J.: Finite Pointset Method (FPM): meshfree flow solver with applications to elastoplastic material laws. In: Oñate, E., Owen, D.R.J. (eds) Proceedings of International Conference on Particle Based Methods: Fundamentals and Applications, Particles 2009, CIMNE, pp. 423–426 (2009)

Kuhnert, J.: Meshfree numerical scheme for time dependent problems in fluid and continuum mechanics. In: Sundar, S. (ed.) Advances in PDE Modeling and Computation, pp. 119–136. Ane Books, New Delhi (2014)

Kuhnert, J., Ostermann, I.: Finite Pointset Method (FPM) and an application in soil mechanics. In: Pardo-Igúzquiza, E., Guardiola-Albert, C., Heredia, J., Moreno-Merino, L., Durán, J., Vargas-Guzmán, J. (eds.) Mathematics of Planet Earth. Lecture Notes in Earth System Sciences, pp. 815–818. Springer, Berlin (2014)

Lim, K.-W., Andrade, J.E.: Granular element method for three-dimensional discrete element method calculations. Int. J. Numer. Anal. Methods Geomech. **38**(2), 167–188 (2014)

Medicus, G., Fellin, W., Kolymbas, D.: Barodesy for clay. Géotech. Lett. **2**, 173–180 (2012)

Medicus, G., Kolymbas, D., Fellin, W.: Proportional stress and strain paths in barodesy. Int. J. Numer. Anal. Methods Geomech. **40**(4), 509–522 (2016)

Medicus, G., Fellin, W.: An improved version of barodesy for clay. Acta Geotech. **12**(2), 365–376 (2017)

Michel, I., Kuhnert, J.: Meshfree numerical simulation in soil mechanics with the Finite Pointset Method (FPM). In: Schaeben, H., Tolosana Delgado, R., van den Boogaart, K.G., van den Boogaart, R. (eds) Proceedings of IAMG 2015 Freiberg, pp. 652–658 (G0102) (2015). ISBN 978-3-00-050337-5 (DVD)

Michel, I., Kuhnert, J., Kolymbas, D.: Meshfree simulation of avalanches with the Finite Pointset Method (FPM). Geophysical Research Abstracts, vol. 19, EGU2017-13203, EGU General Assembly 2017, Vienna (2017)

Murakami, A., Setsuyasu, T., Arimoto, S.: Mesh-free method for soil–water coupled problem within finite strain and its numerical validity. Soils Found. **45**(2), 145–154 (2005)

Obermayr, M., Dressler, K., Vrettos, C., Eberhard, P.: A bonded-particle model for cemented sand. Comput. Geotech. **49**, 229–313 (2013)

Obermayr, M., Vrettos, C.: Anwendung der Diskrete Elemente Methode zur Vorhersage von Kräften bei der Bodenbearbeitung. Geotechnik **36**(4), 231–242 (2013)

Oñate, E., Idelsohn, S.R., Celigueta, M.A., Rossi, R., Marti, J., Carbonell, J.M., Ryzhakov, P., Suárez, B.: Advances in the particle finite element method (PFEM) for solving coupled problems in engineering. In: Oñate, E., Owen, R. (eds.) Particle-Based Methods, pp. 1–49. Springer, Dordrecht (2011)

Oñate, E., Labra, C., Zárate, F., Rojek, J.: Modelling and simulation of the effect of blast loading on structures using an adaptive blending of discrete and finite element methods. In: Escuder-Bueno, I., Altarejas-García, L., Castillo-Rodríguez, J.T., Matheu, E. (eds.) Risk Analysis, Dam Safety, Dam Security and Critical Infrastructure Management, pp. 365–371. Taylor & Francis Group, London (2011)

Ostermann, I., Kuhnert, J., Kolymbas, D., Chen, C.-H., Polymerou, I., Šmilauer, V., Vrettos, C., Chen, D.: Meshfree generalized finite difference methods in soil mechanics—part I: theory. Int. J. Geomath. **4**, 167–184 (2013)

Pastor, M., Haddad, B., Sorbino, G., Cuomo, S., Drempetic, V.: A depth-integrated, coupled SPH model for flow-like landslides and related phenomena. Int. J. Numer. Anal. Methods Geomech. **33**, 143–172 (2008)

Peng, C., Wu, W., Yu, H., Wang, C.: A SPH approach for large deformation analysis with hypoplastic constitutive model. Acta Geotech. **10**(6), 703–717 (2015)

Polymerou, I.: Untersuchung großer Verformungen in der Vertushka. PhD Thesis, University of Innsbruck, Logos Verlag Berlin GmbH (2017)

Schenkengel, K.-U., Vrettos, C.: Modelling of liquefaction-induced lateral spreading using the Lattice Boltzmann method. In: Proceedings 5th International conference on Earthquake Geotechnical Engineering, Paper No MOLSC-922621417 (2011)

Schneider-Muntau, B., Chen, C.-H., Bathaeian, S.M.I.: Simulation of shear bands with Soft PARticle Code (SPARC) and FE. Int. J. Geomath. **8**, 135–151 (2017)

Sloan, S.W., Nazem, M., Zakrzewski, N., Cassidy, M.: On application of the maximum entropy meshless method for large deformation analysis of geotechnical problems. Appl. Mech. Mater. **846**, 331–335 (2016)

Soga, K., Alonso, E., Yerro, A., Kumar, K., Bandara, S.: Trends in large-deformation analysis of landslide mass movements with particular emphasis on the material point method. Géotechnique **66**(3), 1–26 (2015)

Suchde, P., Kuhnert, J.: Point cloud movement for fully Lagrangian meshfree methods. (2017) arXiv:1704.00618

Suchde, P., Kuhnert, J., Tiwari, S.: On meshfree GFDM solvers for the incompressible Navier–Stokes equations. (2017) arXiv:1701.03427

Suchde, P., Kuhnert, J., Schröder, S., Klar, A.: A flux conserving meshfree method for conservation laws. Int. J. Numer. Methods Eng. (2017). doi:10.1002/nme.5511

Tiwari, S., Antonov, S., Hietel, D., Kuhnert, J., Wegener, R.: A meshfree method for simulations of interactions between fluids and flexible structures. In: Griebel, M., Schweitzer, M.A. (eds.) Meshfree Methods for Partial Differential Equations III, pp. 249–264. Springer, Berlin (2007)

Tiwari, S., Kuhnert, J.: A meshfree method for incompressible fluid flows with incorporated surface tension. Revue Eur. Élém. **11**(7–8), 965–987 (2002)

Tiwari, S., Kuhnert, J.: Finite Pointset Method based on the projection method for simulations of the incompressible Navier–Stokes equations. In: Griebel, M., Schweitzer, M.A. (eds.) Lecture Notes in Computational Science and Engineering, vol. 26, pp. 373–387. Springer, Berlin (2002)

Tiwari, S., Kuhnert, J.: Grid free method for solving poisson equation. In: Rao, G.S. (ed.) Wavelet Analysis and Applications, pp. 151–166. New Age International Publishers, New Delhi (2004)

Tiwari, S., Kuhnert, J.: A numerical scheme for solving incompressible and low mach number flows by Finite Pointset Method. In: Griebel, M., Schweitzer, M.A. (eds.) Lecture Notes in Computational Science and Engineering, vol. 43, pp. 191–206. Springer, Berlin (2005)

Tiwari, S., Kuhnert, J.: Modeling of two-phase flows with surface tension by Finite Pointset Method (FPM). J. Comput. Appl. Math. **203**(2), 376–386 (2007)

Tramecon, A., Kuhnert, J.: Simulation of advanced folded airbags with VPS-PAMCRASH/FPM: development and validation of turbulent flow numerical simulation techniques applied to curtain bag deployments. SAE Technical Paper 2013-01-1158 (2013) doi:10.4271/2013-01-1158

Tootoonchi, A., Liu, G.R., Khalili, N.: A cell-based smoothed point interpolation method for flow-deformation analysis of saturated porous media. Comput. Geotech. **75**, 159–173 (2016)

Uhlmann, E., Gerstenberger, R., Kuhnert, J.: Cutting simulation with the meshfree Finite Pointset Method. Procedia CIRP **8**, 391–396 (2013)

Vermeer, P.A., Beuth, L., Benz, T.: A Quasi-static method for large deformation problems in geomechanics. In: Proceedings 12th IACMAG, pp. 55–63 (2008)

Wu, C.T., Chen, J.S., Chi, L., Huck, F.: Lagrangian meshfree formulation for analysis of geotechnical materials. J. Eng. Mech. **127**(5), 440–449 (2001)

Zhu, H.H., Miao, Y.B., Cai, Y.C.: Meshless natural neighbour method and its application in elasto-plastic problems. In: Liu, G., Tan, V., Han, X. (eds.) Computational Methods, pp. 1465–1475. Springer, Berlin (2006)